Available online at www.sciencedirect.com
SCIENCE DIRECT®
Acta Materialia 53 (2005) 2581–2594
Acta MATERIALIA
www.actamat-journals.com

Study of atom diffusivity and related relaxation phenomena in Fe_3Al–(Ti,Nb)–C alloys

I.S. Golovin [a,*,1], S.V. Divinski [b], J. Čížek [c], I. Procházka [c], F. Stein [d]

[a] Institute for Materials, Technical University of Braunschweig, Langer Kamp 8, D-38106, Braunschweig, Germany
[b] Institute for Materials Physics, University of Münster, Münster, Germany
[c] Faculty of Mathematics and Physics, Charles University, Prague, Czech Republic
[d] Max-Planck-Institut für Eisenforschung GmbH, Düsseldorf, Germany

Received 15 December 2004; received in revised form 3 February 2005; accepted 4 February 2005
Available online 2 April 2005

Abstract

Mechanical spectroscopy, positron annihilation spectroscopy (PAS), and the radiotracer diffusion technique (^{59}Fe self-diffusion measurements) were applied to interpret anelastic relaxation effects caused by C atoms and vacancies in Fe_3Al-based alloys with and without strong carbide forming elements (Ti and Nb). The decrease of the Snoek-type relaxation peak (denoted as S-peak) in the internal friction (IF) spectra of Fe–26Al–(2&4)Ti and Fe–26Al–0.3Nb alloys with respect to the S-peak in binary Fe–26Al alloy (all compositions in at.%) is related to a decrease in the amount of interstitially dissolved C atoms. Kinetic aspects of the removal of C atoms from the solid solution are discussed with respect to the annealing temperature. The so-called X peak, which is observed in the IF spectra of Fe–26Al alloy, also almost disappears after alloying with Ti. The results indicate that the change in the content of interstitially dissolved C is the main reason for the observed changes of the S and X peak intensities. The effect of heat treatments on thermal vacancy concentration is evaluated by PAS. A minor influence of the addition of Ti and Nb on the total concentration of vacancies is deduced from the positron annihilation and radiotracer diffusion studies.

Keywords: Iron aluminides; Alloying; Internal friction; Radiotracer diffusion; Positron annihilation

1. Introduction

Anelastic diffusion-related effects in Fe_3Al-based alloys are of special interest in view of possible technological applications of Fe–Al intermetallic compounds as structural materials at moderate and elevated temperatures. The carbon-, aluminium- and vacancy-related internal friction (IF) relaxation peaks in a wide range of Fe–Al compositions have been discussed in a recent review [1]. Three IF relaxation peaks are observed in Fe_3Al above room temperature [2]: the Snoek-type peak (denoted as the S peak), the so-called X peak, and the Zener (Z) peak. The presence of Al in Fe significantly influences the S peak with respect to its original parameters in α-Fe [3]. The peak is shifted to higher temperatures and becomes broader as a result of C–Al long-range 'elastic' interactions [4,5]. Ordering phenomena in Fe–Al are known to decrease the S peak width: this effect was recently very clearly observed in an alloy with 20 at.% Al [6].

The S and Z peaks appear in Fe–Al alloys at a wide range of Al concentrations, while in earlier studies the X peak was only observed in alloys with high Al content [1,4]. The X peak was observed for the first time in Fe_3Al in [7], where it was noted that the X relaxation is observed

* Corresponding author.
E-mail address: i.golovin@tu-bs.de (I.S. Golovin).
[1] On leave from Physics of Metals and Materials Science Department, Tula State University, Tula, Russia.

1359-6454/$30.00
doi:10.1016/j.actamat.2005.02.017

only if relatively low resonance frequencies are employed to test as quenched (from 950 K and higher) specimens which were not subjected to ageing before the measurements. Both carbon atoms and vacancies were supposed to contribute to this relaxation peak [2,5,7]. The contribution of vacancies to the formation of the S and X peaks (the peaks were called differently in original papers) was suggested in [8,9] mainly on the basis of positron annihilation results [8], while in most of the earlier papers at least the S peak is explained as the Snoek-type relaxation (as reviewed in [1]). The vacancy and interstitial atom interaction in an Fe–40%Al alloy and their competing contribution to the hardness of the alloy at different temperatures are discussed in [10]. The dissociation of the C-vacancy complexes is reported to occur in the temperature range around 700 K which is not substantially higher than the X peak relaxation measured with the resonance frequency below 1 kHz.

The effect of alloying (Ti, Nb < 2%) on the relaxation peaks in Fe_3Al was reported in [1,2]. A pronounced decrease of the S and X peaks in respective ternary alloys was related to a strong influence of the carbide-forming elements Ti and Nb on the C concentration in the pertinent solid solutions. Nevertheless, in our previous papers we have not considered: (i) the possible influence of Ti and Nb atoms on the vacancy concentration, and (ii) the influence of ageing on the amount of C atoms in interstitial positions in Fe_3Al.

The effect of heat treatments and alloying elements on the vacancy concentration can be studied directly by positron annihilation and indirectly by radiotracer self-diffusion measurements, since a change in the local vacancy concentration has to influence the diffusivity of the matrix atoms. Self-(Fe) and solute (Ni, Co, Mn, In, Zn, Cr) diffusion in binary Fe_3Al has already been intensively studied by the radiotracer diffusion technique [11–13]. Recently, new data on Al diffusion in this intermetallic compound were derived from interdiffusion studies [14,15].

In the present paper, we study carbon atom diffusion in the Fe_3Al-based intermetallic alloys Fe–26Al, Fe–26Al–(2&4)Ti and Fe–26Al–0.3Nb by IF measurements, the vacancy concentration in respective alloys after different heat treatments by positron annihilation spectroscopy (PAS), and the effect of the alloying elements on Fe radiotracer self-diffusion in these alloys.

2. Materials and experimental techniques

2.1. Materials preparation and microstructures

Four alloys based on $D0_3$-ordered Fe–26Al (compositions given in at.% throughout) with compositions given in Table 1 were prepared by induction melting in argon inert gas from the pure elements Fe (99.95 wt%), Al (99.999 wt%), Ti (99.9 wt%), and Nb (99.9 wt%). The Fe, Al, and Nb contents were analysed by electron-probe microanalysis (EPMA) giving good agreement with the nominal compositions within 0.2 at.%. The impurity contents of one alloy (Fe–26Al) were determined by chemical analyses as $c_O = 0.015$, $c_N = 0.006$, $c_P < 0.003$, $c_S < 0.001$, and $c_{Si} < 0.002$ at.%. The C contents as obtained from chemical analysis are included in Table 1.

Table 1
Compositions of the studied alloys

Alloy	Al (at.%)	C (at.%)	Nb (at.%)	Ti (at.%)
Fe–26Al	25.8	0.006	–	–
Fe–26Al–0.3Nb	26.0	0.003	0.3	–
Fe–26Al–2Ti	26	<0.01	–	2
Fe–26Al–4Ti	26	<0.01	–	4

The values for the Ti-containing alloys are nominal compositions, the other values are from analyses by EPMA (Fe, Al and Nb) and chemical analyses (C).

The microstructures of the as-cast alloys were studied by light optical microscopy and transmission electron microscopy (TEM). All alloys investigated are single-phase materials based on the $D0_3$-ordered intermetallic compound Fe_3Al. The ternary additions Ti and Nb are known to occupy the Fe_I sites (4(b) sites in Wyckoff notation) of the $D0_3$-ordered structure; see, e.g. [16]. Thermal analysis by DTA (differential thermal analysis) showed that the temperature of the second-order transition from $D0_3$- to B2-ordering in Fe–26Al (818 K) is strongly increased by the ternary additions [17]. The TEM investigations ensured that the alloys were completely $D0_3$-ordered when annealed for 45 min at 773 K [17]. The grain sizes of the polycrystalline material varied in the range 200–500 μm. In the Ti containing alloys Ti-carbides were found which appear as isolated, cube-shaped precipitates with dimensions up to 1 μm and have a cubic crystal structure (Fig. 1).

The specimens for IF measurements were sealed in evacuated silica ampoules, annealed at 1273 or 1523 K for 20 min, and immediately water-quenched. We used two different types of cooling: ''type I'' cooling was simply immersing the silica ampoules with the specimens into cold water, while ''type II'' cooling was immersing the silica ampoules with the specimens into cold water and crashing them immediately, which was supposed to result in a higher cooling rate.

For the RD measurements, the cylindrical samples of 9 mm in diameter were cut from 3 mm thick plates by spark-erosion. One face of the specimen was polished to mirror-like quality by a standard metallographical procedure. The samples were wrapped in Ta foil, sealed in silica tubes under purified Ar atmosphere (10^2 Pa), and annealed at 1373 K for 24 h in order to remove the mechanical stresses, which could have built up and which could affect the diffusion behaviour. In addition,

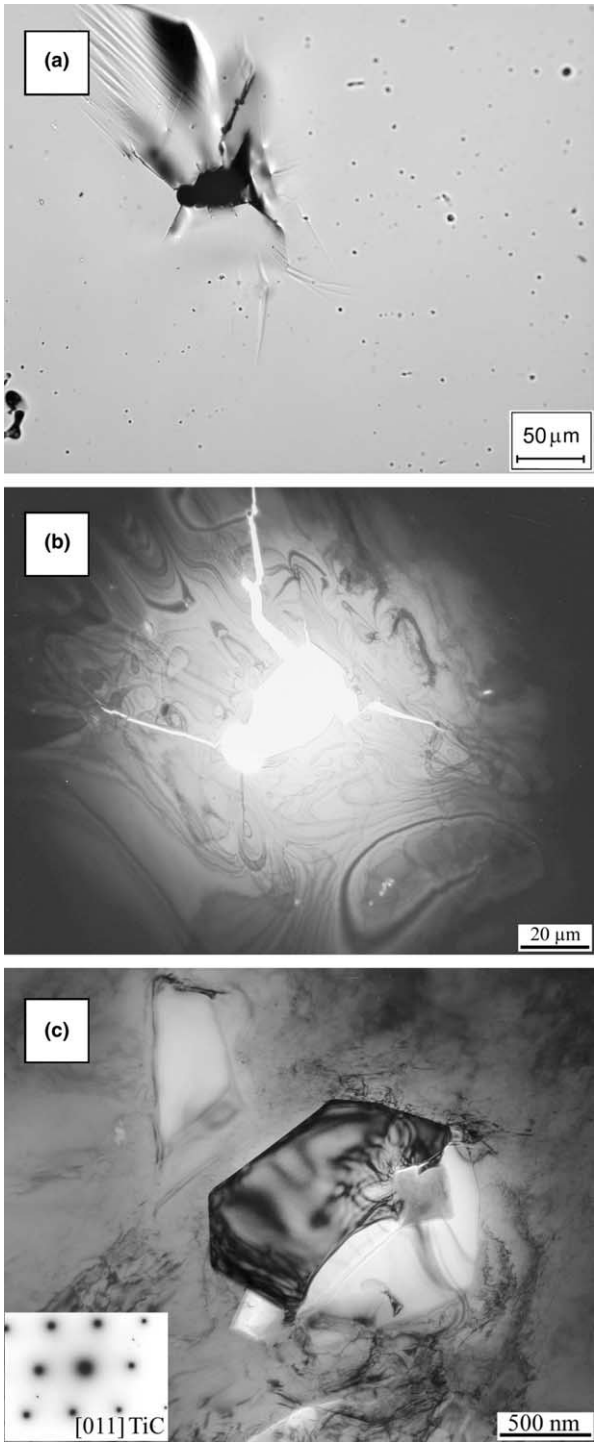

Fig. 1. (a) Light-optical micrograph of a TEM-film of Fe–26Al–4Ti showing a large number of TiC precipitates about 1 μm in diameter in the matrix; (b) TEM bright field micrograph of the same region showing the TiC precipitates in the thinned region around the TEM hole; (c) enlarged section of the same region showing a typical TiC precipitate and the corresponding electron diffraction pattern which can be clearly indexed with the face-centered cubic structure of TiC.

after the pre-annealing, the prepared surface was slightly chemically polished with Syton to remove the effects of thermal etching.

Specimens for positron annihilation $10 \times 10 \times 0.5$ mm^3 in size were cut from the same materials, and quenched from 1273 and 1523 K similarly to the IF specimens.

2.2. Experimental techniques

2.2.1. Internal friction study

Two different mechanical spectroscopy techniques were used:

1. The vibrating-reed apparatus with free decay method for damping measurement (IMNF Technical University of Braunschweig [18]) in a vacuum of about 10^{-3} Pa was used to measure internal friction (IF) of bar-shaped specimens ($30 \times 2 \times 0.4$ mm^3). Basic bending oscillations were measured in the frequency range from 200 to 600 Hz applying optical detection. The amplitude of vibrations was typically less than 10 μm at the free end of the reed, corresponding to a maximal strain of $\varepsilon_0 \approx 10^{-5}$ in the surface region.
2. An inverted torsion pendulum (RKM-TPI, Tula [19]) was applied at lower frequencies using the free-decay method with working frequencies in the range from 1 to 3 Hz. The samples, which were rectangular bars of $70 \times 1 \times 1$ mm^3 in size, were studied in vacuum of ≈1 Pa under a maximum surface deformation of $\gamma_0 \approx 3 \times 10^{-5}$. A magnetic field of up to 2×10^4 A/m could be additionally applied.

The applied heating rate was 1 K/min in all experiments.

2.2.2. Positron annihilation spectroscopy

Two complementary techniques of positron annihilation spectroscopy (PAS) were employed in the present work:

1. Positron lifetime (PL) measurements were performed using a fast–fast configuration of the spectrometer described in [20] with timing resolution of 170 ps (full width at half maximum (FWHM) of the timing resolution function for ^{22}Na, i.e., energies of 1274 and 512 keV for the start and the stop photons, respectively) at a coincidence count rate of 100 s^{-1}. At least 10^7 counts were accumulated in each PL spectrum. Decomposition of PL spectra into exponential components was performed using a maximum likelihood procedure [21].
2. Coincidence Doppler broadening (CDB) studies were employed by a CDB spectrometer consisting of two HPGe detectors and commercial NIM modules operated by a PC. The energy resolution of the spectrometer was 1.1 keV (FWHM) at 512 keV energy and the coincidence count rate amounted to ≈650 s^{-1}. At least 10^8 events were collected in each two-dimensional

spectrum, which was subsequently reduced into a one-dimensional Dopper-broadened profile and instrumental resolution cuts [22]. In order to inspect the nature of positron annihilation sites, relative changes of Doppler profiles were followed as ratios of normalised counts to a proper reference profile. The reference profile was taken to be well annealed (defect-free) high purity α-Fe (99.999%).

A carrier-free ^{22}Na positron source with activity 1.5 and 1 MBq was used for PL and CDB measurements, respectively. The positron source was in both cases sealed between 2 μm thick mylar foils.

2.2.3. Radiotracer diffusion measurements

The radiotracer ^{59}Fe (half-life 45 d) was produced by neutron irradiation of enriched (to about 71%) stable isotope ^{58}Fe at the research reactor GKSS in Geesthacht, Germany. The activated isotope material was dissolved in diluted HCl and then further diluted with double-distilled water.

The radiotracer ^{59}Fe was dropped on the prepared face of the samples. The samples were wrapped into Ta foil to avoid any undesirable contamination. The specimens were sealed in silica tubes under purified Ar atmosphere ($\sim 10^2$ Pa) and subjected to the given diffusion anneals. The temperatures were measured and controlled with Ni–NiCr thermocouples with an accuracy of about ±1 K. After the diffusion annealing, the samples were reduced in diameter (at least 1–2 mm) by grinding to remove the effect of lateral and surface diffusion.

The penetration profiles were determined by the precision grinding sectioning technique using special abrasive mylar foils. The radioactivity of each section was determined with a liquid scintillation counter TRI CARB 2500 TR. The penetration profiles present the plots of the normalised activity of each sections (the activity divided by the weight of the section) vs. the penetration depth x. The latter was calculated from the weight loss of the sample with known geometry after each sectioning step. The density of the samples was carefully measured. Further details of improved sectioning and counting procedures can be found in [23].

The uncertainties of individual points on the penetration profiles, stemming from the counting procedure and the errors of the depth determination, were estimated to be typically less than 10%.

3. Results and discussion

3.1. Temperature-dependent internal friction

The temperature-dependent internal friction (TDIF) spectra, which were measured at two different frequencies (≈2 and ≈200 Hz) in Fe–26Al, Fe–26Al–2Ti, Fe–26Al–4Ti, and Fe–26Al–0.3Nb alloys, are presented in Fig. 2. Three relaxation IF peaks can be distinguished in the binary Fe–26Al alloy above room temperature: the S peak, the X peak, and the Z peak. The temperature dependency of the resonance frequency (only for tests at about 200 Hz) and the heat flow effect are also plotted in Fig. 2(b) in order to show (i) the phase transformations of as quenched Fe–26Al from disordered A2 to ordered $D0_3$ and the second order transformation from $D0_3$ to B2 order, and (ii) the well known decrease in modulus ($E \sim f^2$) within each relaxation process (peak), known as Kronig–Kramers function. A mechanical loss peak in case of a relaxation effect with a single relaxation time is well-known to be described by a Debye equation [24]

$$Q^{-1} = \Delta \cdot \frac{\omega\tau}{1+(\omega\tau)^2}, \tag{1}$$

where τ is the relaxation time, Δ is the relaxation strength, $\omega = 2\pi f$ with f being the frequency of the mechanical vibrations. It is usual to measure Q^{-1} as a function of temperature (T), i.e., TDIF. The jumps of atoms are the elementary steps of their diffusion, and their temperature dependence is described by the

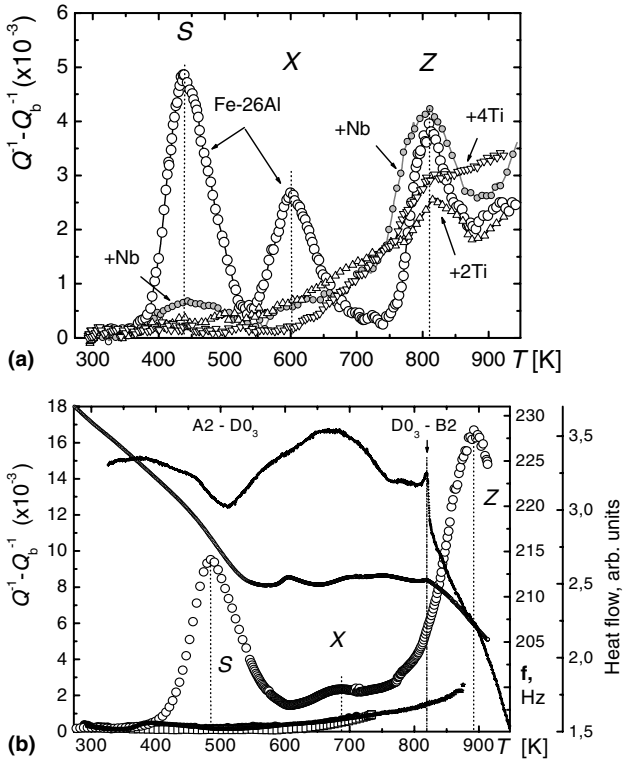

Fig. 2. Temperature-dependent internal friction curves (after background subtraction) showing the S, X, and Z peak positions in the Fe–26Al (open circles), Fe–26Al–0.5Nb (filled circles), Fe–26Al–2Ti (up triangles), and Fe–26Al–4Ti (down triangles) alloys at low (~2 Hz, (a)) and high (~230 Hz, (b)) frequency. In (b), temperature dependent resonance frequency (elastic modulus $E \sim f^2$) and heat flow curves are shown (two left scales) in order to illustrate the ranges of ordering (heat flow) and elastic properties.

Arrhenius equation: $\tau^{-1} = \tau_\infty^{-1}\exp(-H/kT)$, where H is the activation energy. For a fixed frequency and a single relaxation time, the temperature dependence of Q^{-1} is described by

$$Q^{-1}(T) = Q_m^{-1}\cosh^{-1}\left\{\frac{H}{R}\left(\frac{1}{T}-\frac{1}{T_m}\right)\right\}, \quad (2)$$

where R is the gas constant and T_m and Q_m^{-1} are the peak temperature and height, respectively.

An example of such a peak is the well-known Snoek peak in α-Fe [3]. In Fe-based alloys, a set of non-equivalent energy positions for atoms and a whole spectrum of relaxation times exists. A variety of particular distribution functions were developed for the description of different alloys. The most widely used one is the Gaussian distribution of a variable $z = \ln(\tau/\tau_m)$, where τ_m is the mean relaxation time

$$\Phi(z) = \frac{\exp\left\{-(z/\beta)^2\right\}}{\beta\sqrt{\pi}} \quad (3)$$

with β being a parameter characterising the width of the relaxation time distribution.

The resulting damping spectrum is broader than a single Debye peak (see Eq. (1))

$$Q^{-1} = \Delta\int_{-\infty}^{\infty}\Phi(\ln\tau)\cdot\frac{\omega\tau}{1+(\omega\tau)^2}\,\mathrm{d}(\ln\tau). \quad (4)$$

This phenomenon is discussed in many papers. The resulting loss spectrum is broader than a single Debye peak and an IF peak can be described with respect to temperature as [25]:

$$Q^{-1}(T) = Q_m^{-1}\cosh^{-1}\left\{\frac{H}{Rr_2(\beta)}\left(\frac{1}{T}-\frac{1}{T_m}\right)\right\}. \quad (5)$$

Here $r_2(\beta)$ represents the relative peak width, i.e., the peak width with respect to the single Debye peak with $\beta = 0$. Values of β for the S peak in different Fe–Al alloys are given in Fig. 5 in [1]. For a quenched Fe–25Al alloy, β is about 2.

For the analytical description of a relaxation peak the parameters Q_m^{-1}, T_m, β, and H have to be known. However, these parameters for the S peak in the Fe–Al alloys are not constants but depend on the type of heat treatment and the temperature of the peak. The reason for the latter dependence is that initially partly disordered material, which had been quenched from high temperatures outside the $D0_3$ stability range, again starts to order at the temperatures where the IF experiments are performed. Since the S peak as any relaxation peak shifts to higher temperatures with increase of the resonance frequency (see Fig. 2), ordering of quenched specimens takes place in the same temperature range in which the S peak is recorded in the case of high-frequency measurements. Introducing the temperature and time dependent parameter η, which describes the degree of ordering, and taking into account that the value Q_m^{-1} depends on the C content in the solid solution, which is also temperature and time dependent, Eq. (5) can be written in the form

$$Q^{-1}(T) = Q_m^{-1}(\eta, C)\cosh^{-1}\left\{\frac{H(\eta)}{Rr_2(\beta(\eta))}\left(\frac{1}{T}-\frac{1}{T_m(\eta)}\right)\right\}. \quad (6)$$

The apparent activation enthalpies of the S and X peak are determined from the frequency–temperature shift of the peak positions to be about 110 and 152 kJ/mol, respectively. The peak widths are $\beta_S \approx 2.1$ and $\beta_X \approx 1.0$ if measured at a low frequency.

The S and X peaks are not observed in the ternary Fe–26Al–(2 and 4)Ti alloys and they are very small in the ternary Fe–26Al–0.3Nb alloy (Fig. 2(a)). This can be explained by trapping of carbon atoms from interstitial positions in solid solution to titanium (Fig. 1) or niobium carbides: Ti and Nb are known to be strong carbide forming elements in iron. A similar effect, i.e., a drastic reduction in the S- and X-peak heights, takes place if 0.1%Zr is added to Fe–Al alloys. This will be discussed in another paper.

The Zener peaks of the Fe–26Al and Fe–26Al–0.3Nb alloys are rather similar (Fig. 2(a)), only the peak width of the ternary alloys is slightly higher. The activation enthalpy in both cases is about 225 kJ/mol. The Zener peak is lower in case of Fe–26Al–2Ti and is practically not observable for Fe–26Al–4Ti. This tendency can be explained by the stabilisation of $D0_3$ ordering by Ti and Nb as both significantly increase the $D0_3$/B2 transition temperatures (0.3Nb: 849 K, 2Ti: 942 K, 4Ti: 1046 K), and the Zener peak height strongly decreases with increase in order. The increase in the Zener peak height in Fe–26Al in high-frequency measurements (Fig. 2(b)) with respect to low-frequency ones is a result of the increase in the peak temperature (at ≈2 Hz it is located at ≈810 K while at ≈210 Hz it is at ≈890 K). Therefore, the Zener peak in Fe_3Al at 2 Hz is measured in the $D0_3$ range, while it is shifted to the B2 range at 210 Hz.

We have also examined the influence of the cooling rate on the IF spectra. For alloys quenched from 1523 K, there is practically no change of the parameters of the Zener peak and only a small increase of the peak heights of the Snoek and X peaks of about 5–10%. If the alloys were quenched from 1273 K, this latter difference is bigger and amounts to about 20–30%.

Supposing that the S peak is caused by jumps of carbon atoms under stress in the Fe–Al solid solution, and applying the well-known relation between the diffusivity D and the relaxation time τ_r for body-centered cubic lattices (a is the lattice parameter) [24]

$$D = a^2/36\tau_r, \quad (7)$$

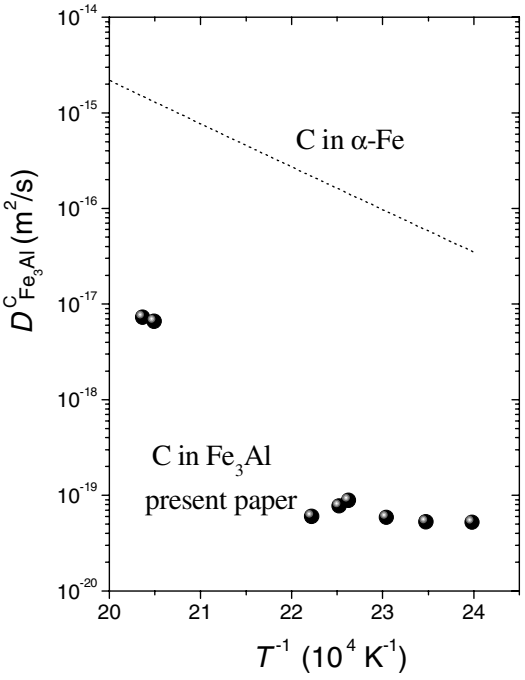

Fig. 3. Arrhenius diagram for carbon diffusion in Fe_3Al (spheres, present paper) compared to α-Fe (dashed line [26]).

the C diffusivity in Fe_3Al can be estimated. In Fig. 3, the diffusion coefficients of C in Fe_3Al (D^{C}_{Fe3Al}) are compared with those of C in α-Fe [26]. It can be seen that C diffusion is much slower in Fe_3Al than in α-Fe presumably due to C–Al long-range 'elastic' interactions.

The results of the above IF studies can be shortly summarised: three IF peaks are recorded in Fe_3Al above room temperature, namely the Snoek-type, the X, and the Zener peak. The S and X peak become significantly smaller or even vanish if Ti or Nb are added to Fe_3Al. The reason supposed is trapping of C atoms in carbides as both Ti and Nb are strong carbide forming elements. At this stage it is not clear whether Ti or Nb change the vacancy concentration in Fe_3Al or not. The parameters of the third peak, i.e., the Zener peak, also strongly depend on the Ti content. The reason is the degree of ordering as Ti significantly increases the order–disorder temperature.

3.2. Positron annihilation

PL spectra of all the studied Fe–26Al and Fe–26Al–4Ti samples can be well fitted by two exponential components (except for the source contribution): a shorter weak component and a longer one with dominant intensity. The shorter component exhibits a lifetime τ_1 in the range 10–30 ps. It represents a contribution of free positrons. The second component with lifetime τ_2 comes from positrons trapped at quenched-in vacancies and represents the dominant contribution to the PL spectra. The lifetimes τ_2 of the second component (listed in Table 2) are similar for all the studied samples and are comparable with the lifetimes reported in the literature for positrons trapped at vacancies in Fe–Al [27,28]. Only a moderate decrease of τ_2 is observed for the samples quenched faster, i.e., directly into water, and from higher temperature (1523 K). Although, this variation could be due to a weak contribution of divacancies, it is clear that quenched-in vacancies represent the dominant positron traps in the studied samples. In the further analysis, it is assumed that the component with lifetime τ_2 comes from positrons trapped at vacancies.

The positron trapping rate K to quenched-in vacancies can be calculated using the two-state simple trapping model (STM) [29]

$$K = \frac{I_2}{I_1}\left(\frac{1}{\tau_f} - \frac{1}{\tau_2}\right), \tag{8}$$

where I_1 and I_2 represent the relative intensities of the shorter and the longer component, respectively, and $\tau_f = (I_1\tau_1^{-1} + I_2\tau_2^{-1})^{-1}$ is the lifetime of positrons annihilating from the free state. The trapping rates calculated using Eq. (8) are given in the fifth column of Table 2.

Table 2
Positron lifetime results

Specimen	Heat treatment (K)	State	τ_2 (ps)	K (10^{10} s^{-1})	c_V (10^{-4} at^{-1})
Fe–26Al	wq 1273, in ampoule	From B2	181.5 ± 0.2	3.2 ± 0.3	0.8 ± 0.1
	wq 1273, in water	From B2	180.8 ± 0.1	5.9 ± 0.5	1.5 ± 0.1
	wq 1523, in water	From A2	179.2 ± 0.1	7.0 ± 0.5	1.7 ± 0.1
Fe–26Al–4Ti	wq 1273, in ampoule	From B2	180.7 ± 0.1	3.2 ± 0.3	0.8 ± 0.1
	wq 1273, in water	From B2	178.0 ± 0.1	6.1 ± 0.5	1.5 ± 0.1
	wq 1523, in water	From A2	175.5 ± 0.1	6.9 ± 0.5	1.7 ± 0.1
Fe–26Al	wq 1273, in ampoule	From B2	181.5 ± 0.2	3.2 ± 0.3	0.8 ± 0.1
	+493, 1 h	$D0_3$ ordering	182.3 ± 0.1	3.2 ± 0.3	0.8 ± 0.1
	+493, 9 h	$D0_3$ ordering	182.5 ± 0.1	3.0 ± 0.3	0.75 ± 0.09
	+493, 40 h	$D0_3$ ordering	182.7 ± 0.2	2.0 ± 0.3	0.49 ± 0.09
	+748, 30 min	$D0_3$ ordering	181 ± 2	0.07 ± 0.02	0.017 ± 0.005

τ_2 represents the lifetime of positrons trapped at quenched-in vacancies; K denotes the positron trapping rate to the vacancies calculated using the STM; c_V is the vacancy concentration calculated by Eq. (9).

The concentration c_V of quenched-in vacancies is directly proportional to the trapping rate

$$c_V = \frac{K}{\nu_V}. \quad (9)$$

The scaling factor ν_V represents the specific positron trapping rate for vacancies in Fe–Al. In the present work, we used a value of $\nu_V = 4 \times 10^{14}\ s^{-1}$ which was reported in [27]. Vacancy concentrations obtained from Eq. (9) are given in the last column of Table 2. It is clear that the samples quenched from 1273 K without breaking the ampoule, i.e., with the slower quenching rate, exhibit a lower concentration of quenched-in vacancies. The specimens quenched from 1273 K with the faster quenching rate (ampoule broken in water) exhibit almost a two times higher concentration of quenched-in vacancies. Thus, the increase in cooling rate helps to fix better thermal vacancies in solid solution at room temperature. On the other hand, quenching from a higher temperature (1523 K) led only to a slight increase of vacancy concentration despite the fact that the equilibrium concentration of thermal vacancies at 1523 K is 4.5 times higher than at 1273 K. The quenching rate is most probably not fast enough to achieve a higher increase of concentration of quenched-in vacancies.

From comparison of PL results for Fe–26Al and Fe–26Al–4Ti samples, we can conclude that the presence of Ti has no influence on the concentration of quenched-in vacancies. This clearly demonstrates that neither the S nor the X internal friction peaks (Fig. 1) can be explained by vacancies as proposed in [6]. The concentration of vacancies does practically not depend on the Ti content in Fe_3Al, while the S and X peak heights critically depend on the Ti content. In Ti containing Fe_3Al alloys the titanium carbides are clearly seen in TEM pictures (Fig. 1).

Isothermal annealing at 493 K shows that the removal of quenched-in vacancies is a rather slow process. This is in agreement with a relatively high vacancy migration enthalpy [28]. Annealing at 493 K for 10 h has practically no influence on the population of the quenched-in vacancies, see Table 2. However, a remarkable decrease of the vacancy concentration was detected after an additional annealing for 40 h at 493 K. Subsequent annealing at 748 K led to a dramatic reduction of the number of quenched-in vacancies. One can see from Table 2 that the concentration of quenched-in vacancies was reduced by factor of ≈30 after annealing at 748 K for 30 min, while the structure is practically completely $D0_3$ ordered.

In order to obtain information about the local chemical environment of the positron trapping sites, the Fe–26Al and Fe–26Al–4Ti samples were studied by CDB spectrometry. In Fig. 4, we show a CDB ratio profile for Fe–26Al quenched from 1273 K in ampoule with respect to the reference α-Fe sample. Very similar profiles were obtained for all the other samples. Thus, the CDB ratio profile shown in Fig. 4 is discussed in the following text as an illustrative example. The CDB ratio profile measured on well-annealed (defect-free) pure Al (99.9999%) is plotted in Fig. 4 as well. It is clear that the CDB profile for the Fe–26Al sample reproduces well the pure Al profile in the high momentum region, i.e., the local minimum at $12 \times 10^{-3}\ m_0c$ and a

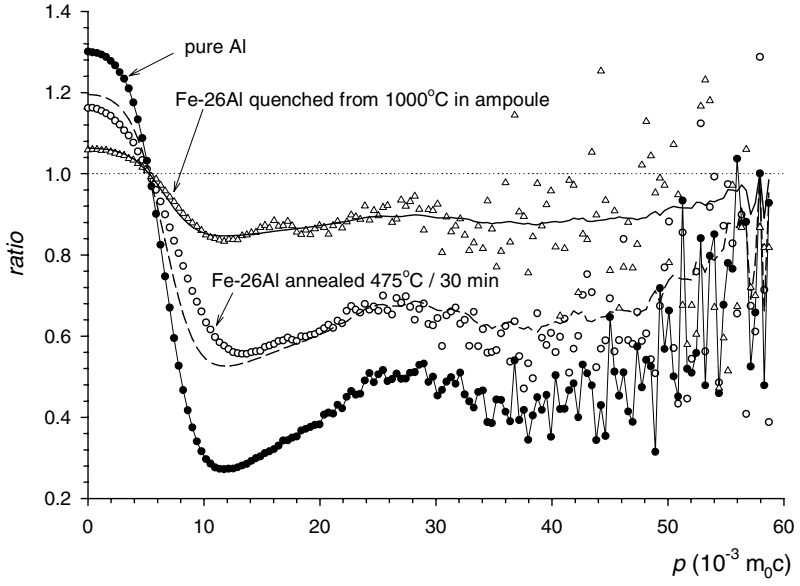

Fig. 4. The CDB ratio profiles (with respect to pure Fe) for pure defect-free Al (filled circles), Fe–26Al quenched from 1273 K in ampoule (open circles), and Fe–26Al annealed at 748 K for 30 min (open triangles). The CDB profiles were symmetrised and only the parts corresponding to the positive Doppler shifts are plotted. Curves corresponding to 65% (dashed line) and 21% (solid line) fraction of positrons annihilating with Al electrons are plotted in the graph as well.

maximum at 25×10^{-3} m_0c. This indicates that the CDB ratio for the Fe–26Al sample comes from positrons annihilating with electrons from the electron shells of Al atoms. By comparison with the pure Al sample (i.e., 100% contribution of positrons annihilating with Al electrons), we determined that the fraction of positrons annihilating with Al electrons in the Fe–26Al sample amounts to $\rho \approx 65\%$, see the solid line in Fig. 4. It is significantly higher than the atomic concentration of Al in the sample. Hence, there is a strong preferential annihilation of positrons with Al electrons. This can be explained by the high density of quenched-in vacancies. It is known that the thermally formed vacancies in $D0_3$-ordered Fe–Al occupy predominantly Fe sites [29]. A high contribution of positron annihilations with Al electrons indicates that vacancies are located mostly on the Fe II sites (with four Fe and four Al atoms as nearest neighbours) rather than on Fe I sites (with eight nearest neighbour Fe atoms). As the majority of positrons are trapped at vacancies, they annihilate in the vicinity of the nearest neighbour Al atoms. The fraction of positrons ξ annihilating from the trapped state in vacancies can be calculated from the PL results using the expression

$$\xi = \frac{K}{K + \frac{1}{\tau_f}}. \tag{10}$$

In case of Fe–26Al quenched from 1273 K in ampoule, one obtains $\xi \approx 80\%$. A contribution of free positrons to the positron fraction ρ annihilating with Al electrons is then $(1 - \xi)\ 0.26 \approx 5\%$. The net fraction of positrons annihilating with Al electrons amounts to

$$\rho = (1 - \xi)0.26 + \xi p_{\mathrm{Al}}, \tag{11}$$

where p_{Al} represents a probability that a positron trapped in a vacancy annihilates with an electron from the electron shell of an Al atom. Using Eq. (11) with $\rho \approx 65\%$ measured by CDB, see Fig. 4, one obtains $p_{\mathrm{Al}} \approx 75\%$. This clearly indicates a strong contribution of annihilations of trapped positrons with electrons from the electron shells of Al atoms surrounding the vacancy. It should be mentioned that the CDB profile for Fe–26Al differs from that of pure Al in the low momentum region (below 12×10^{-3} m_0c). This is due to a high concentration of vacancies in the Fe–26Al sample, while the reference Al is a defect-free material. This difference results in different contributions of positron annihilations with low-momentum delocalised electrons.

Annealing at 748 K led to a significant decrease of the contribution of positrons annihilating with Al electrons. The CDB ratio profile for the annealed sample can be reasonably approximated assuming $\rho \approx 21\%$, see Fig. 4. From the PL results for the annealed sample using Eq. (10) we obtained the fraction of positrons annihilating from the trapped state $\xi \approx 7\%$. Hence, assuming $p_{\mathrm{Al}} \approx 75\%$ derived for the as-quenched sample in the previous paragraph, we obtained from Eq. (11) the net fraction of positrons annihilating with Al electrons $\rho \approx 24\%$. This is in reasonable agreement with the value of $\rho \approx 21\%$ measured by CDB for the annealed sample, see Fig. 4. The decrease of the contribution of positron annihilations with Al electrons is in agreement with the dramatic decrease of the vacancy concentration after annealing at 748 K, see Table 2.

The results of the PL investigations described above can be briefly summarised as follows. The samples quenched from 1273 K in ampoule exhibit the lowest concentration of vacancies. There is only a slight difference in the vacancy concentrations between the samples quenched from 1273 to 1523 K. This agrees very well with the results of the IF experiments. Most of the thermal vacancies occupy Fe II sites with four Fe and four Al atoms as nearest neighbours. Low temperature annealing (473–748 K) decreases the vacancy concentration in binary Fe_3Al. At 473 K, this process is very slow, while at 748 K, it only needs a few minutes to eliminate the thermal vacancies. The presence of Ti in Fe_3Al has no practical influence on the vacancy concentration in the quenched states. This demonstrates that neither the S nor the X internal friction peak (Fig. 2) can be explained by vacancies because the heights of the S and X peaks critically depend on the Ti content. In Ti containing Fe_3Al alloys, titanium carbides are clearly seen in TEM pictures (see Fig. 1).

3.3. Radiotracer diffusion measurements

The diffusion study was performed in the temperature interval of 948–1124 K within the B2 ordered region of the corresponding bulk phase diagrams [17,30]. The alloys with applied tracer were annealed in the same silica tube to eliminate possible slight differences in the annealing temperature. Thus, the established diffusivities can directly be compared.

The penetration profiles measured in the present work are shown in Fig. 5 as a function of the penetration depth in terms of the Gaussian ($\ln c$ vs. x^2) solution. After an initial bulk-diffusion-induced part, all penetration profiles show extended grain boundary induced parts. The profiles were numerically fitted accounting for both, bulk and grain boundary (GB) diffusion. In Fig. 5, the penetration profiles corrected for the GB diffusion contribution are presented.

The bulk diffusivity D_{v} was determined from the slope of the $\ln c$ vs. x^2 curves

$$D_{\mathrm{v}} = \frac{1}{4t}\left(\frac{\partial \ln c}{\partial x^2}\right)^{-1}. \tag{12}$$

The experimental parameters (temperatures and times of diffusion anneals) and the results are summarised in Table 3.

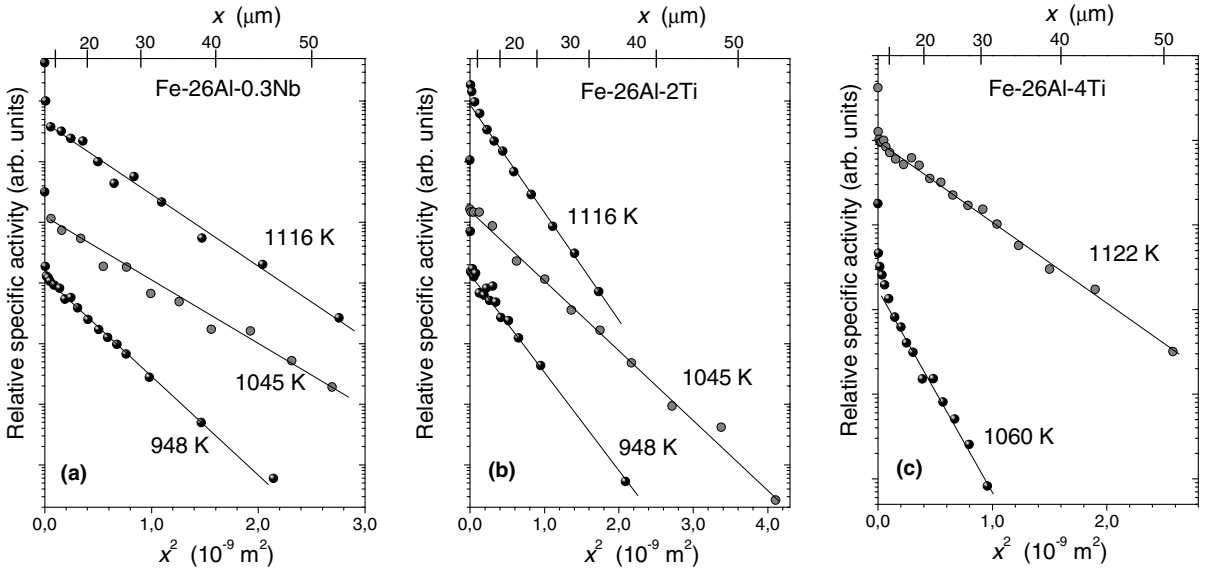

Fig. 5. Penetration profiles of ^{59}Fe diffusion in (a) Fe–26Al–0.3Nb, (b) Fe–26Al-2Ti, and (c) Fe–26Al–4Ti alloys; x is the penetration depth.

Table 3
Parameters of ^{59}Fe diffusion in polycrystalline Fe_3Al-based alloys

T (K)	t (s)	D_v (m^2/s)
Fe–26Al		
1055	158,400	1.59×10^{-15}
Fe–26Al–0.3Nb		
948.2	1,198,500	6.03×10^{-17}
1045.0	158,400	5.78×10^{-16}
1115.5	10,800	5.70×10^{-15}
Fe–26Al–2Ti		
948.2	1,198,500	5.44×10^{-17}
1045.0	158,400	6.27×10^{-16}
1115.5	10,800	8.28×10^{-15}
Fe–26Al–4Ti		
1059.8	143,850	7.62×10^{-16}
1122.3	8640	5.20×10^{-15}

T and t are temperature and time of diffusion anneals, respectively; D_v is the bulk diffusivity.

Fe diffusion in Fe_3Al alloy was thoroughly measured by Eggersmann and Mehrer [11]. Since the composition in that study (27 at.% Al) was slightly different from that of the present binary alloy (25.8 at.% Al), we have re-measured Fe diffusion in Fe–26Al at $T = 1045$ K. The present value is consistent with the previous one (1.56×10^{-15} vs. 1.23×10^{-15} m^2/s, respectively; see Fig. 6) and the slight difference could be a result of the difference in composition.

The addition of Ti and Nb to the Fe–26Al alloy hardly changes the absolute magnitude of Fe bulk diffusion (Fig. 6). The Arrhenius parameters of the Fe diffusion in the Fe_3Al-based alloys are summarised in Table 4. Since Fe diffusion in the Fe–26Al–4Ti alloy was measured only at two temperatures in a relatively narrow

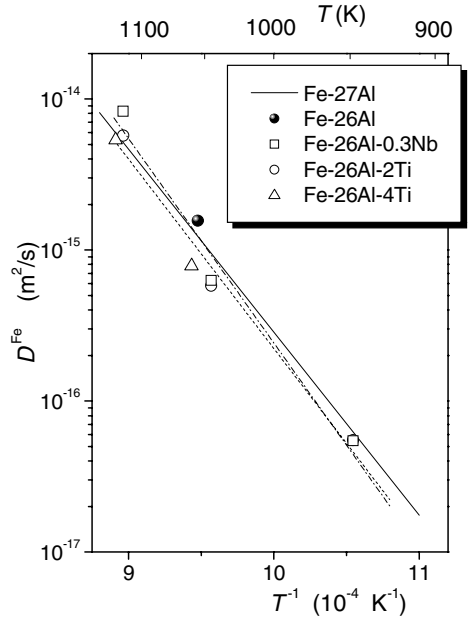

Fig. 6. Arrhenius diagram for ^{59}Fe diffusion in Fe–26Al–0.3Nb (squares and dashed-dotted line) and Fe–26Al–2Ti (circles and dashed line) alloys in comparison to Fe self-diffusion in Fe–27Al (solid line [11] and black point (present paper)).

Table 4
Arrhenius parameters of ^{59}Fe diffusion in the Fe_3Al based alloys

Alloy	D_0 (m^2/s)	ΔH_{Fe} (kJ/mol)	Reference
Fe–27Al	3.8×10^{-4}	232	[11]
Fe–26Al–0.3Nb	8.35×10^{-3}	259 ± 30	Present paper
Fe–26Al–2Ti	7.8×10^{-4}	240 ± 21	Present paper

D_0, the pre-exponential factor; ΔH_{Fe}, the activation enthalpy.

temperature interval, the corresponding Arrhenius parameters were not determined.

The relatively large uncertainties in the activation enthalpies are due to the restricted temperature interval of the present radiotracer measurements. The activation enthalpy of Fe diffusion in Nb- and Ti-containing alloys is slightly larger than the activation enthalpy of Fe diffusion in Fe_3Al, which according to [11] is 232 kJ/mol in the B2 phase region. This may be a result of higher atomic order in these alloys.

Ti and Nb are typical Fe-substituting elements. Direct measurements indicate that other Fe-substituting elements, such as Ni or Co, diffuse somewhat more slowly than Fe in Fe_3Al with a larger activation enthalpy [12]. Presumably, a similar behaviour has to be expected for Ti and Nb, too. Such an effect is related to an increased energy barrier for atom jumps between Fe and Al sites in ordered aluminides as well as to a size-effect (note that Ti and Nb have larger atomic radii with respect to that of Fe). Then, a certain repulsion between the alloying elements under consideration and the vacancies may be suggested.

The present measurements of Fe diffusion in Fe_3Al-based alloys were performed in the B2 phase region, whereas the IF measurements were confined to the $D0_3$ (the S and X peaks, and also the Zener peak if measured at low frequency) and partially to B2 (the Zener peak if measured at higher frequencies) regions of the corresponding phase diagrams. It is notable that the activation enthalpy of the Zener relaxation, estimated to be about 225 kJ/mol for Fe–26Al alloy, is relatively close but smaller than the activation enthalpy of the ^{59}Fe diffusion in both B2 and $D0_3$ phase regions.

The extensive study of Fe diffusion in Fe_3Al [11] suggests a definite, but relatively small effect of the B2–$D0_3$ ordering on the Fe diffusivity. Thus, the total effect of ordering on diffusion is not dramatic in the present case and the conclusions derived from our high-temperature study may certainly be extended to lower temperatures.

The total effect of addition of Ti or Nb on the vacancy concentration is relatively small and definitely cannot explain the full effect in the decrease of the X peak in the ternary alloys. From these experiments, we can also conclude that the change in C concentration in interstitial positions is the main reason for the observed behaviour, although, a certain effect of Ti and Nb on the total vacancy concentration cannot fully be neglected.

3.3.1. Grain boundary diffusion of Fe in Fe_3Al-based alloys

The second part of the penetration profiles corresponds to a short-circuit diffusion contribution. In the present case of polycrystalline samples, such a contribution originates from grain boundary diffusion. In the present paper, the effect of alloying elements on Fe grain boundary diffusion in Fe_3Al-based alloys is analysed.

The present experimental conditions correspond to the so-called Harrison's B-type [31] regime of grain boundary diffusion. In this case, the grain-boundary-related part of the penetration profiles originates from the tracer atoms which enter the samples via fast grain boundary diffusion with subsequent leakage into the bulk of grains via bulk diffusion. It is important that the bulk diffusion length, $(D_v t)^{0.5}$, is much larger than the grain boundary width δ. According to the general Suzuoka's solution, the grain-boundary-related part has to be linear in the coordinates of $\ln c$ vs. $x^{6/5}$ [32]. This is indeed the case in our experiments.

Then, the product $P = \delta \cdot D_{gb}$ of the grain boundary width δ and the grain boundary diffusivity D_{gb} can be determined from the pertinent slope of this part of the penetration profiles [32]

$$P = 1.084 D_v^{0.469} t^{0.531} \left(\frac{\partial \ln c}{\partial x^{6/5}} \right)^{-1.718}, \quad (13)$$

if the grain boundary diffusion parameter $\beta = \delta D_{gb}/2D_v(D_v t)^{0.5} > 10$.

^{59}Fe diffuses more slowly in Fe–26Al–0.3Nb as well as in both Fe–26Al–2Ti and Fe–26Al–4Ti alloys with respect to Fe grain boundary diffusion in Fe_3Al by a factor of two to three at $T = 1050$ K.

Summarising the results derived by the radiotracer study, we conclude that the magnitude of Fe bulk diffusion in Fe_3Al practically does not change with alloying of up to 4 at.% Ti or 0.3 at.% Nb, whereas an increase in the activation enthalpy ΔH_{Fe} was observed. This effect is attributed to a certain repulsion between the alloying elements and the vacancies (which are mainly vacancies on the Fe sublattice). Addition of both Nb and especially Ti slows down Fe grain boundary self-diffusion, presumably due to their strong segregation at grain boundaries in the alloys.

3.4. Time-dependent internal friction

An important conclusion from Sections 3.2 and 3.3 is that neither the S peak nor the X peak reported in Section 3.1 can be explained by vacancy migration alone as it was suggested in [8] or by Al atom migration which involves vacancy motion [9]. Instead, the existence of these peaks can be mainly related to the presence of carbon in the solid solution. While the mechanism of the X peak could most probably involve complexes of carbon atoms and vacancies in Fe–Al solid solution, the mechanism of the S peak is the Snoek type relaxation [3], as originally proposed by Hren [33], Jäniche et al. [34], Tanaka [35], etc.

This conclusion about the mechanisms of the S and X peaks allows for the study of the effect of ageing temperature and time on carbon content in Fe–Al solid solution. We have carried out long term isothermal annealing of water quenched Fe–26Al alloy with parallel

measurements of IF in the temperature range from 453 to 539 K, i.e., at temperatures where the S peak is pronounced. The following procedure was applied: specimens water-quenched from 1273 K were heated to a chosen temperature from 453 to 539 K (stage 1), then isothermal annealing up to 60 h was performed (stage 2), and subsequently, the specimens were cooled down to room temperature (stage 3). At all these stages the IF was simultaneously recorded. Finally, IF spectra of such a long term annealed specimen were measured again between room temperature and 725 K (stage 4). Stage four is important in order to find out a proper IF background at the temperature of isothermal annealing, i.e., to see clearly IF background at temperatures below and above the peak. Then the value of the IF background Q_b^{-1} for the temperature of the isothermal annealing was subtracted from the time-dependent IF curve: $(Q_t^{-1} - Q_b^{-1})$. Finally, we normalised these isothermal curves $(Q_t^{-1} - Q_b^{-1})$ measured at different temperatures T to the height of the IF value at the very beginning of isothermal annealing after subtraction of the corresponding background $(Q_0^{-1} - Q_b^{-1})$. As a result, the "normalised" isothermal curves $((Q_t^{-1} - Q_b^{-1})/(Q_0^{-1} - Q_b^{-1}))$ vs. t are obtained. Such curves $(Q_t^{-1} - Q_b^{-1})/(Q_0^{-1} - Q_b^{-1})$ vs. time are plotted in Fig. 7(a) for varying temperatures between 453 and 539 K.

The monotonous decrease of the mechanical loss peak with respect to ageing time is attributed to the thermally activated process of removal of point defects, e.g., carbon atoms from solid solution in α-Fe [36], and should correspond to the general dependence

$$k(T) = k_0 \exp(Q/RT), \tag{14}$$

where k_0 (s) is the value of k at infinite temperature and Q is the activation energy of the process of removal of interstitial C atoms.

As has been proven in the above sections, the thermal migration of interstitial C atoms governs (or at least plays the most important role for) the development of the S-peak. The corresponding effective activation enthalpy Q of the thermally activated process of removal of carbon atoms can be estimated using isothermal kinetics at different temperatures (Fig. 7(a))

$$Q = R \times \mathrm{d}(\ln((Q_t^{-1} - Q_b^{-1})/(Q_0^{-1} - Q_b^{-1}))/\mathrm{d}(1/T)). \tag{15}$$

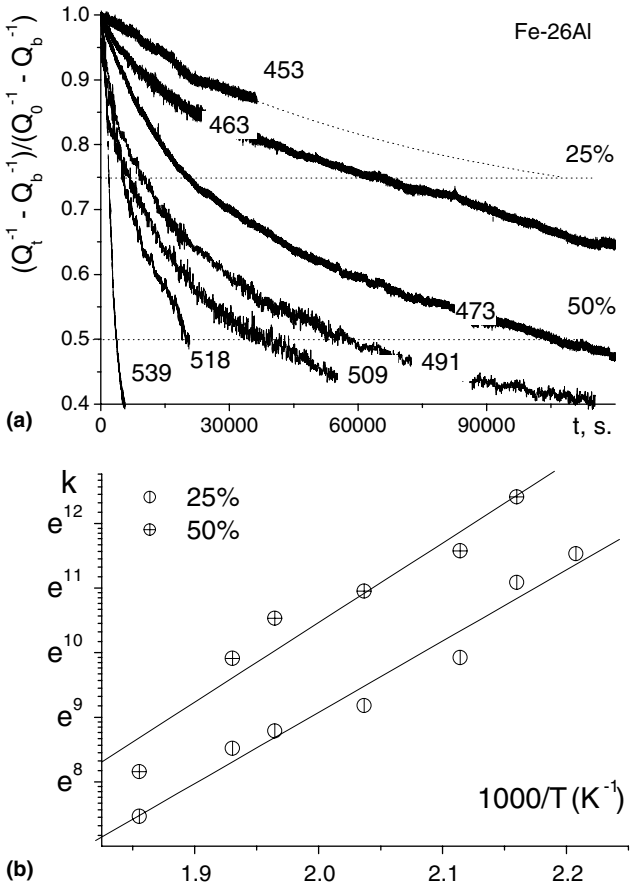

Fig. 7. (a) Isothermal change in the S peak height in the temperature range 453–538 K (values at the curves are temperatures in K); (b) Arrhenius plot for 25% and 50% stages of carbon atom removal from the solid solution.

The activation enthalpy Q of the thermally activated process of removal of carbon atoms in Fe–26Al alloy can be calculated for example for 25% ($Q_{25} \approx 91.5$ kJ/mol) or 50% ($Q_{50} \approx 102.4$ kJ/mol) decrease in the IF peak height, i.e., for 25% or 50% removal of carbon atoms from the solid solution (Fig. 7(b)). The pre-exponential factors in Eq. (14) $k_{0/25/50}$ are about 2.3×10^{-6} or 0.7×10^{-6} s. With an increase in annealing time the kinetics slow down. The mean value of Q (≈96 kJ/mol) at the stage of interstitial solid solution decomposition between 25% and 50% derived from the isothermal annealing measurements roughly agrees with the effective activation enthalpy of carbon diffusion in

Table 5
Activation energies of the process of removal of carbon from solid solution (Q) and carbon atom diffusion under stress (H) in the solid solution $Fe_3Al(C)$

Alloy	Degree of decomposition	Activation energy (Q) determined from isothermal kinetics	Activation energy (H) determined from the S peak	Difference
		Q (kJ/mol)	H (kJ/mol)	$H - Q$ (kJ/mol)
$Fe_3Al(C)$	25%	91.5	109.5	18
	50%	102.4		7.1

Fe_3Al, which is about 109.5 kJ/mol (Table 5). This difference suggests that the thermally activated process of the removal of carbon atoms from the solid solution in Fe–26Al is dominated by a faster process than solely bulk diffusion, presumably by grain boundary or dislocation-enhanced diffusion. Note that a pronounced contribution of grain boundary diffusion was observed even at much higher temperatures of the independent RD measurements in all studied alloys.

The velocity of the removal of C atoms from the interstitial solid solution $Fe_3Al(C)$ is slower than that for a α-Fe(C) solid solution measured using the same experimental technique, i.e., with a resonance frequency of about 250 Hz and $T_m \approx 100$ °C (373 K) [37]. The influence of the Al content on the velocity of the removal of C atoms from the Fe-based solid solution is the subject of another paper [38].

Assuming that the removal of carbon atoms is the only or at least the main effect of annealing of quenched $Fe_3Al(C)$ alloy at 180–265 °C one can analytically solve Eq. (6) if η = constant (no ordering during IF measurements). In the case of the ordinary carbon Snoek peak in α-Fe, the relaxation strength is proportional to the amount of dissolved carbon in solid solution and inverse proportional to the peak temperature. Such a relation is also valid for Fe–Al alloys: in this case we have a distribution of relaxation times (see through Eqs. (1)–(5)), the peak is broadened, and it is more correct to operate not in terms of the Snoek peak height but in terms of area under the Snoek peak [6]. Assuming a simple exponential dependence between the carbon content in the solution and the ageing time (t) at a fixed temperature (T), one can write the time and temperature dependence for a IF value Q_m^{-1} in Eq. (6) as: $Q_m^{-1} = Q_{m0}^{-1}\exp[-t/k(T)]$, where Q_{m0}^{-1} is equal to Q_m^{-1} at $t = 0$ for a given T. Then Eq. (6) can be corrected with respect to carbon content in solid solution as

$$Q^{-1}(T) = Q_{m0}^{-1}(\eta)\exp\left[\frac{t}{\exp(-Q/RT)}\right] \times \cosh^{-1}\left\{\frac{H(\eta)}{R\cdot r_2(\beta(\eta))}\left(\frac{1}{T}-\frac{1}{T_m(\eta)}\right)\right\}. \quad (16)$$

Now the open question is if we can define η as a function of annealing time or even decide that η is constant. TEM investigations of Fe–26Al (Fig. 8) show significant ordering at 473 K which is within the range of our IF study of isothermal processes. In samples quenched from 1273 K, big sized B2 domain antiphase boundaries with very fine $D0_3$ domains inside can be detected (Fig. 8(a)). Annealing for 8 and 100 h at 473 K increases the $D0_3$ domains sizes. This clearly demonstrates that the parameter η in Eq. (16) is time and temperature dependent. At this stage of research we do not have sufficient data to quantify this dependence.

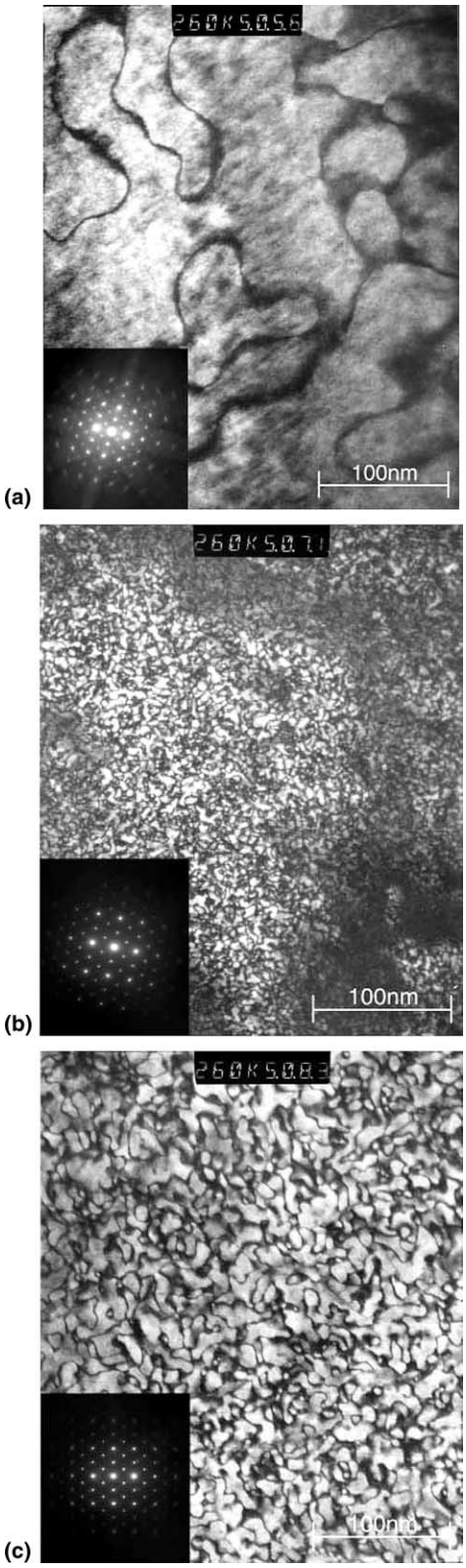

Fig. 8. TEM investigations of Fe–26Al: (a) water-quenched from 1273 K (B2 antiphase boundaries, inside very fine domains of $D0_3$ structure: [1 1 0](2 0 0) dark field); (b) plus 8 h at 473 K ($D0_3$ domains are well distinguishable: [1 1 0](1 1 1) dark field); and (c) plus 100 h ageing at 473 K ($D0_3$ domains are bigger: [1 1 0](1 1 1) dark field): magnification 260,000×.

One can consider the kinetics of ageing of as-quenched $Fe_3Al(C)$ specimens (Fig. 7) not from the viewpoint of how much C is remaining in the solid solution but from the viewpoint of nucleation and growth of precipitates. The theory of such an approach with respect to IF for α-Fe was presented by Wert [39]. The amount of transformed phase $q = \Delta C(t)/C_0$ (C_0 is the initial concentration of solute atoms) is

$$q = 1 - \exp(-t/\tau)^n, \tag{17}$$

where q in terms of the Snoek IF peak is $q = (Q_t^{-1} - Q_b^{-1})/(Q_0^{-1} - Q_b^{-1})$, t is the ageing time, τ is a time constant depending on C_0, and n is an independent parameter, the value of which is connected with the shape of the precipitates. The validity of this approach was confirmed in different papers, e.g., with respect to the precipitation of C in Fe in [40] for different carbon concentrations and different temperatures and times of annealing. In order to find out the value of n for $Fe_3Al(C)$, we plotted $\log(\ln(\Delta C(t)/C_0))$ vs. $\log t$ (see Fig. 9). The resulting values for the parameter n are given in Table 6.

From Fig. 9 and Table 6 one can conclude that the precipitation process can be divided into two stages. The first stage is characterised by $n \approx 1$–0.6, the second one by $n \approx 0.5$. Some uncertainties remain for data at 518 K (only one stage with $n \approx 0.6$). Quantitatively these values might be corrected in future experiments. Nevertheless, the data show two stages: nucleation and growth

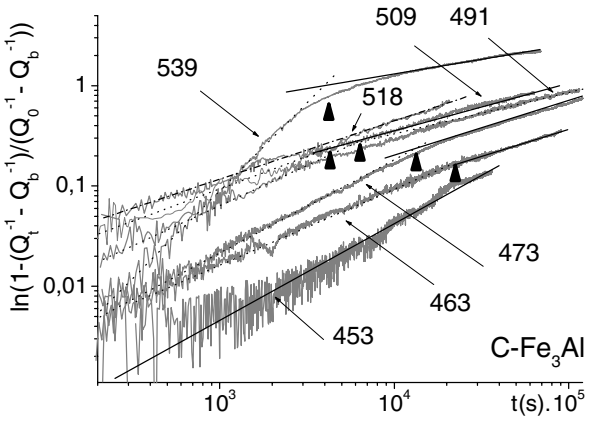

Fig. 9. Ageing after quenching: amount of carbon in precipitates according to the Wert model [39]. The numbers near the curves are the annealing temperatures in K.

Table 6
Values of the parameter "n" in Eq. (17) for Fe–26Al

T (K)	453	463	473	490	590	518
n_1	0.97	0.79	0.90	0.72	0.65	0.59
n_2	No data	0.55	0.47	0.45	0.47	

of carbides. Basically this fits well with our TEM study, where no precipitates were found in as-quenched specimens and after 1 h of ageing at 493 K, while κ-carbides were observed after 8 and 100 h. These results will be a subject of another paper.

The Wert–Zener approach was created for the simple process of carbon (nitrogen) precipitation from α-Fe. In as-quenched Fe_3Al, the process of C atom precipitation is overlapped with at least two more processes: decrease in thermal vacancy concentration (see Table 2) and ordering of Al atoms in iron (Fig. 8). Each of these processes can contribute to C precipitation kinetics, and a differentiation between both processes directly from the IF spectra is not possible. Results of a study of IF spectra as a function of frequency, which will be reported elsewhere, demonstrate that there is some non-thermally activated contribution to the IF spectra in the range of the S peak. This contribution can not be explained by carbon atom jumps in solid solution.

4. Summary and conclusions

The addition of Ti or Nb to Fe–26Al does practically not change the vacancy concentration in the as-quenched state, while it leads to trapping of carbon atoms from the solid solution by the formation of carbides. This latter effect leads to a strong reduction or even vanishing of the S and X relaxation peaks in the temperature dependent IF spectra of quenched specimens of the ternary alloys Fe–26Al–2Ti, Fe–26Al–4Ti and Fe–26Al–0.3Nb. Thus, the mechanism of the underlying relaxation process is the "diffusion under stress" of interstitial C atoms in the Fe–Al solid solution (the Snoek-type peak) and in the vicinity of vacancies (the X peak) but not vacancy reorientation as it has been suggested in several papers. The effective activation enthalpies of the relaxation processes corresponding to the S and X peaks are estimated to be about $H_S = 110$ and $H_X = 152$ kJ/mol, respectively.

A similar but weaker effect of the removal of carbon atoms from the solid solution takes place in the case of long-term ageing. The activation enthalpy of the thermally activated process of the removal of carbon atoms from the solid solution amounts to about $Q = 96$ kJ/mol. Thermal vacancy annihilation takes place already at 493 K, and speeds up at higher temperatures.

^{59}Fe radiotracer diffusion proceeds with similar rates in Fe–26Al, Fe–26Al–2Ti, Fe–26Al–4Ti, and Fe–26Al–0.3Nb alloys. This experimental finding indirectly supports the conclusions of the present positron annihilation study about the minor effect of the alloying elements on the vacancy concentration in the Fe_3Al-based alloys under consideration.

Acknowledgements

The ^{59}Fe isotope production at the nuclear reactor in Geesthacht, Germany is greatly acknowledged. We thank S.B. Golovina (TU-BS), T.S. Pavlova (TSU) and A. Strahl (TU-BS), and C. Grusewski (TU-BS) and E. Bartsch (MPIE) for valuable help with the IF tests and TEM study, respectively. I.S.G. is grateful to H. Neuhäuser and H.-R. Sinning for discussions. Part of this work is supported by DFG projects.

References

[1] Golovin IS, Neuhäuser H, Rivière A, Strahl A. Intermetallics 2004;12:125.
[2] Golovin IS, Golovina SB, Strahl A, Neuhäuser H, Pavlova TS, Golovin SA, Schaller R. Scripta Mater 2004;50:1187.
[3] Snoek JL. Physica VIII 1941;7:711.
[4] Golovin IS, Pozdova TV, Rokhmanov NYa, Mukherji D. Metall Mater Trans A 2003;34:255.
[5] Blanter MS, Golovin IS, Sinning H-R. Scripta Mater 2005;52:57.
[6] Pozdova TV, Golovin IS. Solid State Phenom 2003;89:279.
[7] Golovin IS, Pavlova TS, Golovin SA. Rep Tula State Univ Mater Sci 2003;4:9 [in Russian].
[8] Schaefer HE, Damson B, Weller M, Arzt E, George EP. Phys Stat Solidi (a) 1997;160:531.
[9] Zhou ZC, Han FS, Gao ZY. Acta Mater 2004;52:4049.
[10] Laakmann J, Hartig C, Mecking H. Z Metallkd 2003;94:526.
[11] Eggersmann M, Mehrer H. Philos Mag A 2000;80:1219.
[12] Peteline S, Tanguep Njiokep EM, Divinski S, Mehrer H. Defect Diffus Forum 2003;216–217:175.
[13] Pavlova TS, Golovina SB, Divinski SV, Golovin IS. DIMAT-2004, Krakow [accepted].
[14] Nakamura R, Takasawa K, Yamazaki Y, Iijima Y. Intermetallics 2002;10:195.
[15] Salamon M, Mehrer H. Z Metallkd 2004;95:4.
[16] Fortnum RT, Mikkola DE. Mater Sci Eng 1987;91:223.
[17] Stein F, Schneider A, Frommeyer G. Intermetallics 2003;11:71.
[18] Harms U, Kempen L, Neuhäuser H. Rev Sci Instrum 1999;70:1751.
[19] Golovin SA, Arkhangelskij SI. Problemi Prochnosti 1971;5:120 [in Russian].
[20] Frank S, Rüsing J, Herzig C. Intermetallics 1996;4:601.
[21] Bečvář F, Čížek J, Lešťak L, Novotný I, Procházka I, Šebesta F. Nucl Instrum Meth Phys Res A 2000;443:557.
[22] Asoka-Kumar P, Alatalo M, Ghosh VJ, Kruseman AC, Nielsen B, Lynn KG. Phys Rev Lett 1996;77:2097.
[23] Divinski SV, Hisker F, Kang Y-S, Lee JS, Herzig C. Z Metallkd 2002;93:256.
[24] Nowick AS, Berry BS. Anelastic relaxation in crystalline solids. New York: Academic Press; 1972.
[25] Schaller R, Fantozzi G, Gremaud G, editors. Mechanical spectroscopy Q−1 2001 with applications to materials science. Clausthal, W. Germany: Trans Tech Publ.; 2001.
[26] Da Silva JRG, McLellan RB. Mater Sci Eng 1976;26:83.
[27] Schaefer H-E, Würschum R, Šob M, Žák T, Yu WZ, Eckert W, Banhart F. Phys Rev B 1990;41:11869.
[28] Würschum R, Grupp C, Schaefer H-E. Phys Rev Lett 1995;75:97.
[29] Brandt W. In: Stewart AT, Roellig LO, editors. Positron annihilation. New York: Academic Press; 1967. p. 155.
[30] Kubaschewski O. Iron-binary phase diagrams. Berlin: Springer-Verlag; 1982.
[31] Harrison LG. Trans Faraday Soc 1961;57:597.
[32] Suzuoka TJ. J Phys Soc Jpn 1964;19:839.
[33] Hren JA. Phys Stat Solidi 1963;3:1603.
[34] Jäniche VW, Braunen J, Heller W. Archiv für das Eisenhüttenwesen 1966;37(9):719.
[35] Tanaka K. J Phys Soc Jpn 1971;30:404.
[36] Pascheto W, Johari GP. Metall Mater Trans A 1996;27:2461.
[37] Golovina SB, Golovin IS. Rep Tula State Univ Mater Sci 2004;5:39 [in Russian].
[38] Golovin IS, Golovina SB, Grusewski K, Sinning H-R, Strahl A, Neuhäuser H. RPS-21, Voronezh, Russia [accepted, to be published in Bulletin of Russian Academy of Sciences, Physics Series (Izvestiga RAN, Ser. Phys.)].
[39] Wert CA. J Appl Phys 1949;20:943.
[40] Krishtal MA, Golovin SA. Internal friction and metals structure. Moscow: Metallurgia; 1976. p. 376 [in Russian].